JOURNAL OF MAGNETIC RESONANCE **125,** 43–51 (1997)
ARTICLE NO. MN961084

Strategies for Rapid NMR Rheometry by Magnetic Resonance Imaging Velocimetry

STEPHEN J. GIBBS,*,† DEREK E. HAYCOCK,‡ WILLIAM J. FRITH,‡ STEPHEN ABLETT,‡ AND LAURANCE D. HALL*,§

*Herchel Smith Laboratory for Medicinal Chemistry, Cambridge University School of Clinical Medicine, University Forvie Site, Robinson Way, Cambridge CB2 2PZ, United Kingdom; and ‡Unilever Research, Colworth House, Sharnbrook, Bedfordshire, MK44 1LQ, United Kingdom

Received August 6, 1996; revised November 22, 1996

Strategies for NMR-based rheometry are discussed with particular attention given to ease of implementation, robustness, and measurement speed. The techniques are based on NMR velocimetry of Poiseuille flow, and together with measurements of the pressure drop, the velocimetric data may be processed to yield measures of the shear viscosity over the range of shear rates present in the Poiseuille flow field of the test fluid. Methods for NMR velocimetry are briefly reviewed, and three methods all based on the pulsed-field-gradient technique are compared experimentally; they involve (1) direct two-dimensional imaging of the tube cross section, (2) one-dimensional imaging of a Cartesian projection of the tube cross section followed by Abel inversion to obtain radial profiles, and (3) measurement of the bulk velocity spectrum of the tube cross section and conversion to the radial velocity profile. The second and third of these techniques allow the most rapid measurements (potentially less than one minute) and show promise for on-line NMR rheometry.

INTRODUCTION

Because of its capabilities for imaging optically opaque materials, magnetic resonance imaging is becoming more and more widely used for materials and process characterization. One of the particular attractions of MRI methods is the ability to perform quantitative velocimetry noninvasively and on optically opaque systems. In recent years, magnetic resonance velocimetry (MRV) has been employed for the study of Poiseuille flow of polymer solutions (*1–3*) and suspensions (*4, 5*), flow in porous media (*6*), flow in chemical process equipment (*7, 8*), granular flow (*9*), thermal convection (*10*), and turbulence (*11*). Recently, several groups have reported the use of MRV for studying rheometric capillary and Couette flows (*1, 3, 12–15*). The combination of velocimetric data with pressure drop measurements for capillary flow allows the simultaneous determination of the effective shear viscosity of the fluid under study over nearly the entire range of shear rates (possibly three or four decades) present in the flow field (*1, 12*). Velocimetric rheometry should be distinguished from other NMR studies of rheology which exploit NMR to monitor molecular orientation in certain rheometric flows (*16*). Since the velocimetric approach to rheometry does not require assumptions regarding shear rates and boundary conditions, *NMR rheometry* is a potentially powerful tool for fluid characterization. Further, the NMR technique can be applied to continuous on-line rheometric characterization of process streams over a wide range of shear rates without need for stream interruption or sampling.

The chief difficulties of the NMR rheometry technique, which currently hinder its more widespread use as an analytical tool, are the expense of the equipment and the long measurement times. We address the issue of measurement speed here by examining several strategies for NMR capillary rheometry some of which allow more rapid acquisition of the required velocimetric data, without need for the expensive, high-performance gradient systems necessary for echo-planar imaging. All of the methods involve the determination of radial velocity profiles but differ in the ways in which the raw NMR data are obtained and processed to yield these profiles. The benchmark method for NMR capillary rheometry involves the acquisition of two-dimensional, planar velocity images of the capillary cross section; radial velocity profiles are obtained simply from the planar data by determining radial positions of each pixel in a velocity image. The determination of the planar velocity image usually requires the acquisition of two or more planar, NMR images of the capillary cross section which are sensitized to the fluid velocity to different degrees. The acquisition of those planar images by routine MRI protocols requires substantial instrument time, typically on the order of several minutes, except for the notable cases in which ultra-fast imaging techniques such as echo-planar methods are possible, in which cases acquisition times are on the order of one second. Because the velocity field is axially symmetric, two-dimensional planar

† Present address: National High Magnetic Field Laboratory, Florida State University, 1800 E. Paul Dirac Drive, Tallahassee, FL 32310, and Department of Chemical Engineering, FAMU-FSU College of Engineering, 2525 Pottsdamer Street, Tallahassee, FL 32307.

§ To whom correspondence should be addressed.

1090-7807/97 $25.00

imaging is not required in order to obtain radial velocity profiles; in fact, radial profiles may be inferred from the bulk velocity spectrum of the capillary flow field or from one-dimensional, velocity sensitized, transverse projections of the circular capillary cross section.

In this paper, we briefly review NMR methods for velocity measurement and then consider in more detail methods for NMR capillary velocimetry and rheometry. Specifically, we compare in terms of robustness and speed two-dimensional imaging, projection imaging, and velocity spectrum measurement as techniques for NMR capillary rheometry. We demonstrate each of the methods with rheometry of a Newtonian test fluid of 50% aqueous sucrose. Briefly, we find that the projection-based technique is both robust and rapid; with this method, a complete radial velocity profile (and hence the dependence of the fluid shear viscosity upon shear rate, or *flow curve*) may be obtained in less than a minute.

BACKGROUND AND THEORY

The basis of velocimetric rheometry is that, for fully developed capillary flow, the shear stress (or momentum flux density τ_{rz}) increases linearly from the center of the tube to the wall; hence

$$\tau_{rz} = -\eta \frac{dv}{dr} = \frac{-dP}{dz}(r/2), \qquad [1]$$

where r is the radial coordinate, z is the axial coordinate, v is the axial velocity, P is the fluid pressure, and η is the shear-rate-dependent fluid viscosity. Therefore, by measuring the pressure drop per unit length of capillary and the radial dependence of the shear rate (dv/dr), one can determine the shear-rate dependence of the fluid viscosity η.

The radial dependence of the fluid shear rate may be determined by numerically differentiating the radial velocity profile determined by the NMR measurements. Flow measurements by NMR methods are well established and have been recently reviewed (*17–19*). In NMR flow measurements, position is encoded in either the phase or the magnitude of the local nuclear magnetization, and displacements over a time interval of 1 to 1000 ms are observed. Although magnitude encoding presents some advantages, such as simplicity of implementation, a phase-encoding approach is convenient for precise measurement of displacements. The phase-encoded magnetization may then either be directly measured for the entire sample, or manipulated further to acquire data sufficient for construction of a spatial map, or image, of the phase-encoded magnetization.

In the phase-encoding method, an initial radiofrequency excitation rotates the local nuclear magnetization from its equilibrium orientation aligned with the large applied magnetic field $\mathbf{B}_0$ into the plane orthogonal to the $\mathbf{B}_0$. Magnetization orthogonal to $\mathbf{B}_0$ precesses about the applied field with a frequency $\omega = \gamma B_0$. A subsequent magnetic field gradient pulse of duration δ temporarily changes the local magnetic field according to $\mathbf{B} = \mathbf{B}_0 + \mathbf{r}\cdot\mathbf{g}$ where $\mathbf{B}$ is the local magnetic field, $\mathbf{r}$ is the position vector, and $\mathbf{g}$ is the applied field gradient. The imposition of this spatial field variation causes nuclear magnetization to acquire a differential phase $\phi = \gamma\mathbf{g}\cdot\mathbf{r}\delta$ depending upon position. After a time interval Δ, a pulsed field gradient of opposite polarity is applied; this pulsed gradient together with the first pulsed gradient causes a net phase accumulation of $\phi = \gamma\mathbf{g}\cdot(\mathbf{r} - \mathbf{r}')\delta$, where $\mathbf{r}'$ is the new position of the nuclear magnetization at imposition of the second gradient pulse. The subsequent nuclear magnetization, for which magnitude, phase, and frequency of precession may be detected, is thus

$$A(\mathbf{r}) \approx \int_V A_0(\mathbf{r})\exp[-i\mathbf{K}\cdot(\mathbf{r} - \mathbf{r}')]dV, \qquad [2]$$

where $\mathbf{K} = \gamma\mathbf{g}\delta$ and in the approximation we have neglected motion during the gradient pulses of duration δ. For a Gaussian distribution of displacements about a coherent displacement caused by steady flow, the detected NMR signal is given by (*20*)

$$A \approx A_0\exp(-\mathbf{K}\cdot\mathbf{D}\cdot\mathbf{K}(\Delta - \delta/3) - i\mathbf{K}\cdot v\Delta), \qquad [3]$$

where $\mathbf{D}$ is the diffusion tensor and v is the fluid velocity. Hence, by measuring A for a few values of $\mathbf{K}$, one can deduce estimates of both $\mathbf{D}$ and v.

APPARATUS

Measurements were performed at a magnetic field strength of 2 T with an Oxford Research Systems BIOSPEC 1 imaging console coupled to an Oxford Instruments 31 cm, horizontal-bore superconducting magnet as summarized in Fig. 1. A custom-built saddle-type radiofrequency coil (*21*) was used in conjunction with an 11 cm internal diameter Helmholtz–Golay, custom-built gradient set driven by three pairs of Techron (Model 7560) audio amplifiers to give an approximate maximum gradient strength of 28 G/cm. Gradient pulse waveforms were carefully shaped to provide precise matching of the areas of the opposing pulses used for motion encoding, and gradient magnitudes were calibrated with a water-filled cylinder of precisely known dimensions. Data were transferred to a network of UNIX workstations for processing.

The flow system used has been described previously (*3*); briefly, it consisted of a Cole-Parmer (Model 7521-25) peristaltic pump feeding a 5 liter reservoir through approximately 3 m of polyvinylchloride tubing. Pressure was measured in the headspace of the 5 liter reservoir with a manometer. From the reservoir, fluid entered a precision-bore 4 mm

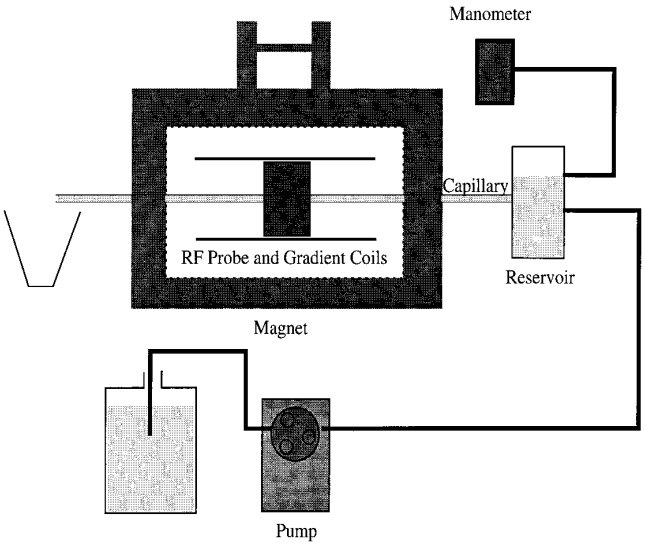

FIG. 1. Schematic of equipment arrangement for NMR capillary rheometry. Fluid is pumped from reservoir containing 47% aqueous sucrose through PVC tubing to a second reservoir and then through the test capillary (1 m long and 4 mm in diameter) before entering a receiver vessel at atmospheric pressure. There are taps in the second reservoir for pressure measurement at a level even with the capillary tube or in the air gap headspace.

i.d. glass capillary (supplied by Chance Brothers Glass, UK) to pass through the center of the horizontal-bore magnet and exit at atmospheric pressure.

COMPARISON OF NMR RHEOMETRY TECHNIQUES

Radial Velocity Profiles from Two-Dimensional, Planar Images

A straightforward approach to NMR flow imaging and rheometry is to acquire a series of flow-encoded, two-dimensional, planar images each with a different value of **K** (aligned parallel with the flow direction) used for flow encoding. A gradient-echo pulse sequence, shown in Fig. 2, with gradient pulses of duration δ for motion encoding, is useful for acquisition of such images (*1, 3*). Two-dimensional, complex Fourier transformation of the acquired data then yields a set of complex images corresponding to the capillary cross section for different values of the motion encoding gradient **g**. Data from each picture element, or pixel, are then fitted using Eq. [3] with the components of **D** and v in the direction of **K** and A_0 as free parameters in order to obtain estimates of the local velocity (*22*).

Radial velocity profiles are then calculated by finding the distance of each pixel in the image from the center of the capillary (*1, 3*). Knowledge of the precise center and dimensions of the pixels is crucial for the calculation of the radial profiles. A procedure based on locating the center from the first spatial moments of a processed image and determining the pixel dimensions from the second central moments of the image has been successful (*1, 3*).

Example image data are shown in Fig. 3 for images corresponding to the imaginary part of the flow-encoded NMR signal. The signal phase changes most rapidly with changing magnitude of **K** in the region of largest velocity at the tube center. Hence, the ring structure in the highly flow-encoded, imaginary channel images can be viewed as contours in $v \cdot \mathbf{K}$. Data were acquired with a relaxation delay between NMR excitations of 500 ms, and with $\Delta = 3.6$ ms, $\delta = 1$ ms, and an average of 32 transients; the time required for the acquisition of each flow encoded image was thus approximately 16 min. The signal-to-noise ratio in the fluid filled region is approximately 15:1, and the spatial resolution is approximately 70 μm.

Also shown in Fig. 3 is the two-dimensional velocity map obtained by regression of Eq. [3] to the data corresponding to $\mathbf{K} = 0$, 10.5, 21, 42.1, 84.2, −84.2, 168, and −168 rad/cm, and the radial velocity profile obtained by azimuthal averaging of two-dimensional velocity map. The azimuthal and radial averaging was performed with a fixed bin size of 50 points, and thus the effective resolution in the radial velocity profile linearly increases from approximately 20 μm at the tube wall to 200 μm at the tube center (*3*). Also plotted are the standard deviations for each bin as error bars on the radial velocity profile.

Radial Velocity Profiles from Velocity Spectra

If the magnitude of the NMR signal A_0 is spatially uniform over the pipe cross section and if the fluid velocity increases

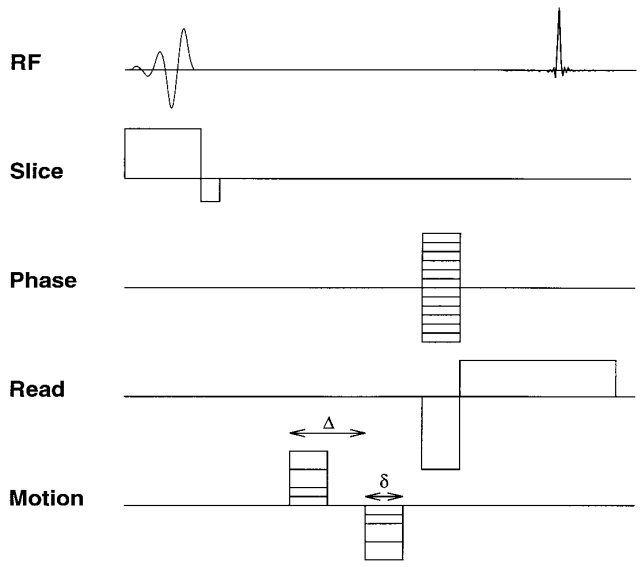

FIG. 2. NMR pulse sequence for flow imaging. The time line shows the series of events in an individual NMR measurement. Each of the five lines represents events happening on a different radiofrequency or gradient channel. The sequence shown here is a gradient-echo sequence with a bipolar gradient pulse pair for flow encoding.

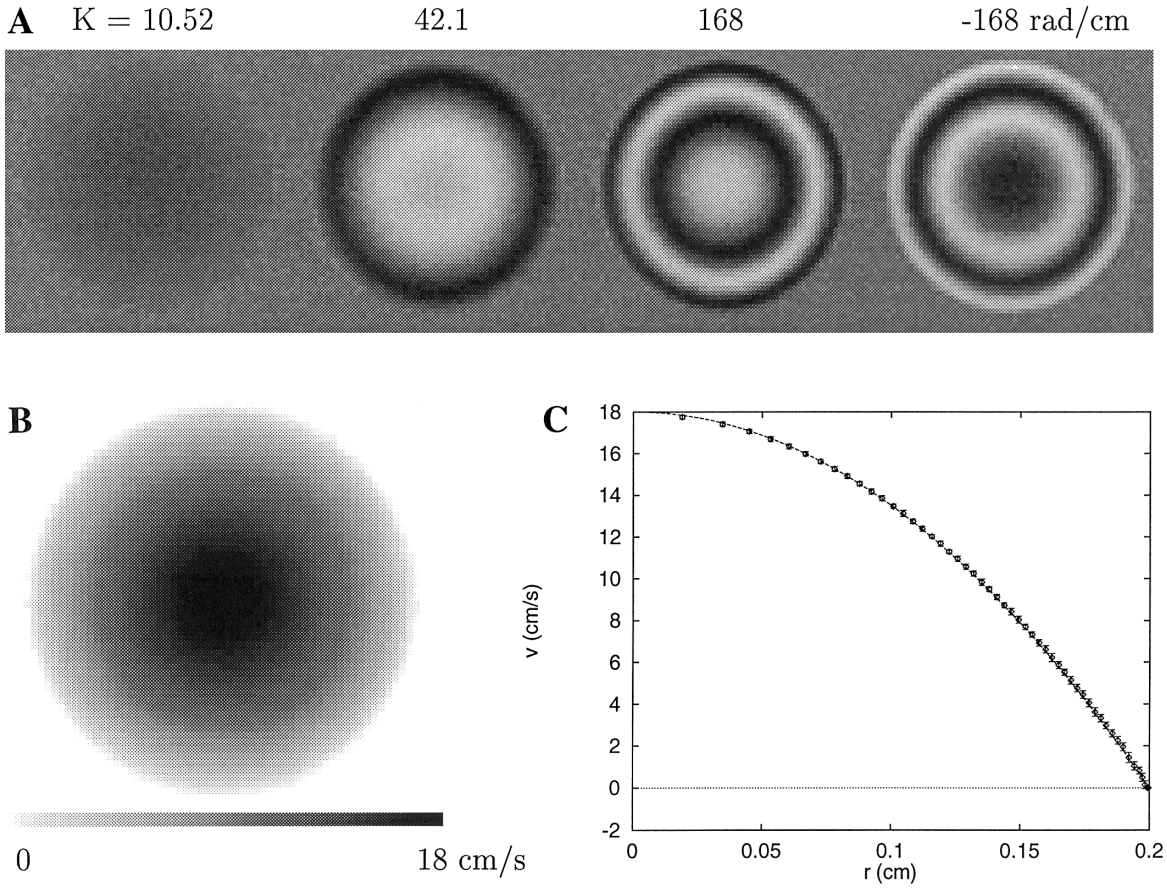

FIG. 3. Two-dimensional flow imaging. Shown are results for a Newtonian fluid, aqueous sucrose solution: (A) Series of flow-encoded images over capillary cross section for four different values of **K** (shown are the imaginary components of Eq. [2]); (B) resulting two-dimensional velocity map obtained by Bayesian frequency analysis of the data in (A); (C) velocity profile obtained from azimuthal averaging of the two-dimensional velocity map, and the expected parabolic velocity profile (best fit with peak velocity as a fitting parameter) for fully developed, laminar, Newtonian flow. Error bars indicate the standard deviations of of bins of 50 points in the radial neighborhood.

monotonically from the wall to the center of the tube, then the bulk velocity spectrum (obtained from the Fourier transform of a series of bulk NMR measurements obtained with incremented values of the motion-encoding gradient) may be transformed to obtain the radial velocity profile.

For the specific case when both the NMR signal intensity A_0 is spatially uniform and there is a monotonically increasing velocity from the wall, the radial velocity profile may be determined without the need for employing any imaging gradients. Instead, the bulk velocity spectrum $S(v)$ may be determined by Fourier transformation of the NMR signal obtained with respect to the motion-encoding gradient, applied in the direction of flow. For the ideal case of spatially uniform nuclear magnetization, the Fourier transform of the motion-encoded signal from the entire tube cross section is the velocity spectrum given (after normalization) by

$$S(v)dv = \int_{r(v+dv)}^{r(v)} 2rdr/R^2, \qquad [4]$$

where $r(v)$ is the radial position associated with a fluid velocity v and R is the tube radius. Hence,

$$S(v)dv = [r^2(v) - r^2(v + dv)]R^{-2} \qquad [5]$$
$$= [-2r(v)dr]R^{-2}.$$

This relationship may be integrated to give

$$\int_{v_{\min}}^{v_i} S(v)dv = \int_{R}^{r(v_i)} - 2r(v)dr/R^2, \qquad [6]$$

where $v_{\min}$ is the minimum velocity present in the spectrum and thus associated with $r = R$, and thus one can assign a radial position to a particular velocity v_i present in the spectrum by

$$r^2(v_i) = R^2\left[1 - \int_{v_{\min}}^{v_i} S(v)dv\right]. \qquad [7]$$

The bulk velocity spectrum data-acquisition scheme does not involve the use of frequency- or phase-encoding magnetic field gradient pulses. There is therefore a potentially large time savings (a factor of N) associated with the elimination of the need for N phase-encoding steps, where N is the number of pixels in the phase-encode direction. Further, this strategy has the potential advantages both of operational simplicity and of reduced noise in the acquired signal because of a reduced acquisition bandwidth. Thus, whereas imaging measurements require magnetic field gradient generation in three orthogonal directions, the procedure outlined here requires magnetic field gradients only in the flow direction. Furthermore, since the data are acquired in the absence of a frequency-encoding gradient, a narrow acquisition bandwidth, on the order of the linewidth of the sample, may be employed, thus improving the signal-to-noise ratio of the acquired signal. These potential benefits must be weighed against the necessity for acquiring data corresponding to about 100 different values of **K** in order that the velocity spectrum may be accurately calculated. It is encouraging to note that Johnson and co-workers (*23*) have used the above method to measure the radial profiles of electro-osmotic flows in capillary tubes.

The assumptions required for unique interpretation of the velocity spectrum may not always be valid. The velocity field may not be axially symmetric if a sufficient entry length for flow development is not allowed. Further, the velocity may not increase monotonically from the wall for time-dependent or pulsatile flows (*24*), and the NMR signal intensity may not be spatially uniform. For example, the magnitude of the local magnetization may depend upon the residence time of the fluid in the polarizing magnetic field if the residence time is short compared to the longitudinal relaxation times of the fluid protons. In these cases, the fluid does not spend sufficient time in the polarizing magnetic field for the nuclear magnetization to reach equilibrium, and hence, the magnetization concentration near the center of the tube, where fluid flow is fastest, may be less than that near the edges. Incomplete polarization may also depend upon the residence time of the fluid in the slice of interest if longitudinal relaxation times are long compared to this residence time and a sufficient relaxation delay is not allowed between successive NMR excitations. Then the NMR signal intensity will be partially saturated depending upon the local velocity and hence dependent on transverse position; specifically, the magnitude of the local magnetization will be less near the edges of the tube than in the center of the tube. It is important to note, however, that the flow-induced nonuniformities in the NMR signal amplitude are usually axially symmetric. Additional inhomogeneity in the NMR signal may result from nonuniformities in the applied static field, the applied field gradients for region selection and motion encoding, and the excitation and detection sensitivities of the radiofrequency coil. All of the above effects will, in general, depend on the fluid velocity and NMR properties.

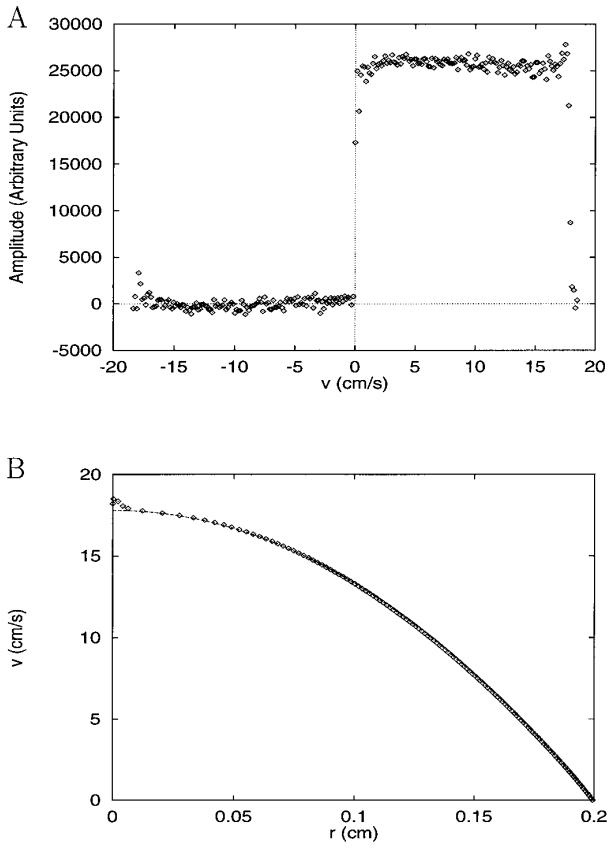

FIG. 4. Velocity spectrum measurement. (A) Velocity spectrum obtained by Fourier transformation of flow-encoded NMR data for the whole pipe cross section with respect to **K**. (B) Velocity profile obtained from processing the velocity spectrum in (A) according to Eq. [7]. Also shown is the parabolic velocity profile (best fit with peak velocity as a fitting parameter) expected for fully developed, laminar, Newtonian flow.

Data were acquired using the same equipment as for the imaging measurements and with the same pulse sequence, with the only exception that the read (frequency-encode) and phase-encode gradients were set to zero. For the velocity spectrum measurement, it is desirable to sample large values of $\mathbf{K}\cdot\Delta$ in order to have adequate velocity resolution in the velocity spectrum. Therefore, larger values of $\delta = 7$ ms and $\Delta = 9.6$ ms were employed. Four signal averages were acquired for each of 256 values of K ranging from -2263 to 2263 rad/cm with a step size of 17.7 rad/cm. Acquisition of the data for the entire velocity spectrum required approximately 30 min (the relaxation delay between NMR transients was lengthened to 2 s to ensure that magnetization near the tube walls was not partially saturated).

The resulting velocity spectrum and velocity profile are shown in Fig. 4. The velocity spectrum is nearly square except for a few points at higher velocities; these give rise to the deviation from the parabolic velocity profile at the

tube center. Further work is required to identify the precise cause of the artifact at higher velocities, but the anomalous points at −18 and 18 cm/s in the velocity spectrum are probably related. It is interesting that the integration procedure involved in generating the velocity profile from the velocity spectrum is insensitive to the noise in the velocity spectrum.

It is also worth noting here that the spectrum measurement technique is ideally suited to the measurement of NMR chemical-shift-resolved velocity profiles; no additional experimental acquisition time is required for measuring the chemical-shift information since the NMR data are acquired in the absence of a read gradient. An important corollary is that there is no chemical-shift-induced spatial misregistration in the velocity profiles obtained by the velocity-spectrum method. Chemical-shift discrimination might find application in on-line measurements of emulsion flow.

Radial Velocity Profiles from One-dimensional Projection Images

One-dimensional projections of the NMR signal corresponding to the pipe cross section are acquired by Fourier transform of an NMR transient acquired in the presence of a *read gradient* precisely oriented orthogonal to the capillary axis. Those flow-encoded projections are then transformed by Abel inversion to obtain the radial dependence of the NMR signal for each of the different flow-encoded projections. The radial data are then analyzed as described above in order to obtain the radial dependence of the fluid velocity and the shear-rate dependence of fluid viscosity.

The basis of the Abel inversion for transforming the acquired projection data to a radial data display is shown in Fig. 5. The projection data are represented by the vector $\mathbf{P}_i$. Hence $\mathbf{P}_0$ represents the NMR signal emanating from the region of the capillary between the lines at X_0 and X_1 of area a_{00}; it is therefore representative of the NMR signal, $S_0 = \mathbf{P}_0/a_{00}$ for a radial position between X_0 and X_1. In order to calculate the signal at the next inward radial position from the projection data, the areas of the regions a_{00} and a_{01} are calculated. The NMR signal corresponding to the radial region between X_1 and X_2 is then given by $S(r_1) = [\mathbf{P}_1 - a_{01}S(r_0)]/a_{11}$; the relationship is not exact because the regions a_{00} and a_{01} do not correspond to precisely the same radial positions. The discrete inverse Abel transform (DIAT) implemented here is, however, computationally simpler than the smoothing, interpolation, and analytical integration procedure described by Majors and Caprihan (*25*).

It should be noted that there is actually some redundancy in the projection data; two projections are available: one for each half of the tube (although one projection may be slightly offset from the other if the center of the tube does not coincide with the center of a pixel). The DIAT algorithm described above treats these two data sets independently; a more robust approach for noisy data might treat the two halves of the tube simultaneously by requiring that the two data sets give radial profiles that vary smoothly in radial coordinate.

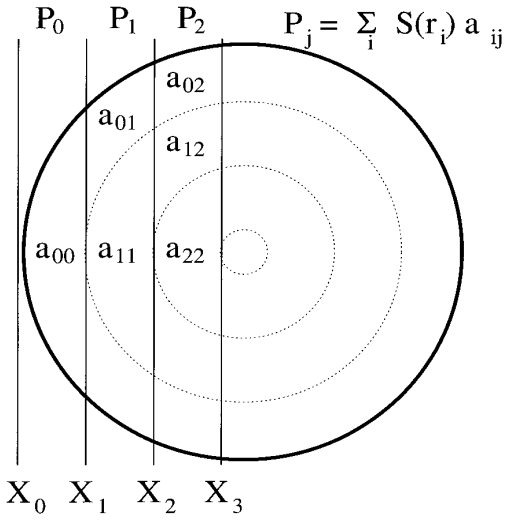

FIG. 5. Schematic illustration of the discrete inverse Abel transform (DIAT) algorithm used for calculating the radial signal $S(r_i)$ from the projection data $\mathbf{P}_j$. The a_{ij} are the areas of the regions bounded by the pixel boundaries X_j and X_{j+1} and circles of radii $r = X_i$ and $r = X_{i+1}$ (the X_j are measured relative to the center of the pipe). The radial signal is calculated starting from r_0 by $S(r_i) = [\mathbf{P}_i - \Sigma_{j=0}^{i-1} S(r_j)a_{ji}]a_{ii}^{-1}$. The $S(r_i)$ are not exact because the a_{ij} correspond to slightly different radial averages for different values of j. In our implementation, the r_i are taken to be $(X_i + X_{i+1})/2$, except for the case of τ_0 in which X_0 is replaced by the pipe radius.

The projection flow imaging technique is illustrated in Fig. 6 for the Newtonian sucrose solution. Figure 6a shows the flow-encoded projection data as a function of **K**, and Fig. 6b shows the flow-encoded radial data obtained from the projection data by the discrete inverse Abel transform as a function of **K**. Two input parameters are required for the DIAT: the location of the center of the capillary tube in the projection direction, and the length of a pixel in the projection direction. It is possible to obtain estimates of these parameters from the projection data, but more accurate estimates are possible using a two-dimensional image of the tube cross section. The center coordinates and pixel dimensions are then obtained from the first and second central moments of an image in which intensities above a certain threshold (chosen to be one-half the average image intensity inside the tube) are replaced by one and those below are replaced by zero (*3*). This procedure eliminates systematic bias resulting from spatially nonuniform radiofrequency excitation or reception.

Figure 6c shows the radial velocity profile determined from these data by Bayesian frequency analysis (*22*) of the data shown in Fig. 6b; the error bars indicate the Bayesian error intervals and the line shows a best-fit parabola, with the peak velocity as the free-fitting parameter. These data

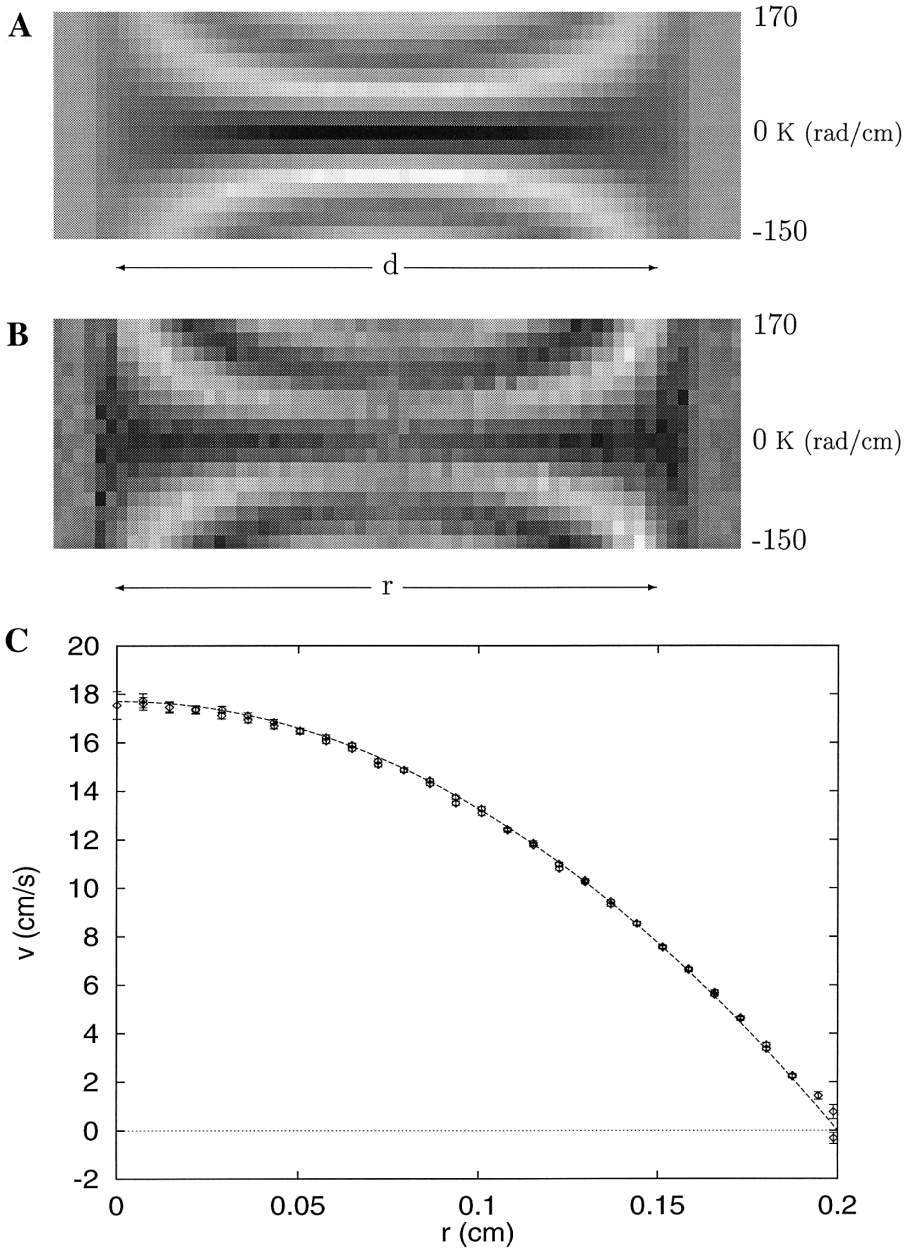

FIG. 6. One-dimensional projection flow imaging. (A) One channel (real part) of phase-corrected, flow-encoded projection data (P_i) as a function of diametral location and K for capillary flow. Black represents positive signal and white represents negative. (B) Radial data ($S(r)$, again real part, as a function of K) obtained by applying the DIAT outlined in the legend to Fig. 5 to the data in (A). (C) Velocity profile obtained by Bayesian frequency analysis of the data shown in (B). The error bars indicate the Bayesian error intervals, and the line is a best-fit parabola (with the peak velocity as the free parameter).

were determined for the same nominal flow rate as for the velocity spectrum and planar-imaging techniques and with $\Delta = 3.6$ ms, $\delta = 1$ ms. The total data-acquisition time was 2 min for 16 signal averages for each of the 16 values of **K** and a repetition delay of 500 ms.

Figure 7 shows a comparison of the shear-rate dependence of the aqueous sucrose viscosity derived from the velocity profiles obtained by the three NMR measurement techniques discussed above using Eq. [1]. All three measurements are consistent with a shear-rate independent viscosity, or Newtonian behavior. The notable outlying points in Fig. 7 correspond to points near the tube center for the velocity spectrum measurement technique and to the points near the tube center and the tube wall for the projection-measurement technique. It is clear from Fig. 7 that the 2-dimensional image-derived data show the least scatter.

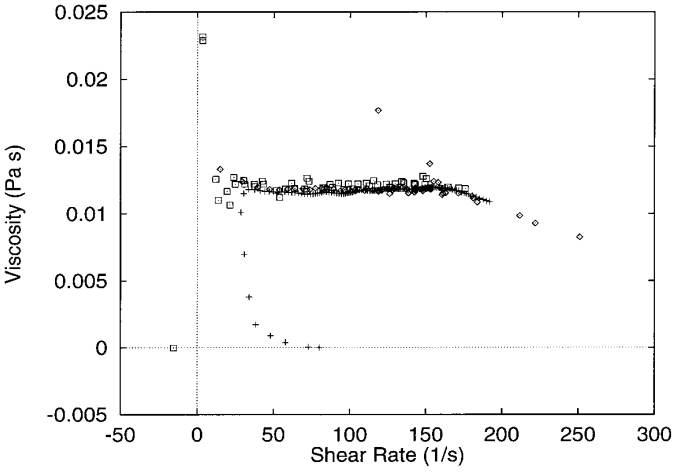

FIG. 7. NMR rheometry: Viscosity as a function of shear rate for the sucrose solution determined by differentiation of the velocity profiles shown in Figs. 3 (diamonds, two-dimensional imaging), 4 (+, velocity spectrum measurement), and 6 (boxes, projection imaging). Data from all three techniques demonstrate Newtonian behavior; the viscosity measurements are largely independent of shear rate except for the large scatter in the projection data (boxes) and the systematic deviation at low shear rates from the spectrum measurement data (+).

DISCUSSION AND CONCLUSIONS

The three measurement strategies outlined above all have potential utility in development and implementation of an on-line NMR rheometry system. The two-dimensional imaging technique is most expensive in terms of both required hardware and measurement time [except for the special cases in which NMR properties of the material under study permit ultrafast imaging (*6*)], but it provides unambiguous velocimetric data by which to check the assumptions of axial symmetry required by the other, less expensive velocimetric techniques. The projection method is potentially the fastest measurement technique, but is inherently noisier than the velocity spectrum technique. Projection-based measurements of velocity profiles, and hence viscosity as a function of shear rate, are possible every few seconds if there is an adequate signal-to-noise ratio in the acquired signal. Otherwise, signal averaging may be necessary, and therefore the slower but less noisy velocity spectrum technique may be competitive if the required acquisition times approach a minute.

It is thus interesting to consider the feasibility of an on-line or in-line NMR rheometer. Such a device might need to be competitive in cost with ruggedized industrial rheometers even though it would offer the advantages of being on-line, of being suitable for monitoring corrosive or dangerous fluids, and of rapidly providing data for a wide range of shear rates. It is thus probable that the NMR rheometer would initially be based on a relatively low-field, permanent magnet (0.2 T) and would not have a high-performance gradient system capable of ultrafast echo-planar imaging. Key operating parameters of such a system would include the length of the polarizing magnet (which need not produce a highly homogeneous field), the length of the homogeneous field regions of the magnet and of the radiofrequency coil, the flow rate, and the pipe diameter. Of primary importance are that the residence time of the fluid in the polarizing region be sufficient with respect to the longitudinal nuclear relaxation time of the species of interest to result in adequate induction of nuclear magnetization and hence signal-to-noise ratios in the acquired data, that the tube diameter be large enough to support adequate signal-to-noise ratios in the measured data, and that flow be laminar.

A preliminary estimate of the feasibility of low-field NMR rheometry can be readily made from the formula of Hoult (*26*) for the signal-to-noise present in the detected signal in a 25 cm diameter radiofrequency coil from a volume V at a frequency ω and with a receiver bandwidth ν:

$$S/N \approx 440\omega V \nu^{-0.5}. \qquad [8]$$

Hence, the S/N available in a 64 pixel projection of a 10 cm i.d. pipe at an NMR frequency of 10 MHz would range from approximately 7:1 at the edge of the pipe to about 50:1 at the pipe center, this, however, corresponds to a S/N of only 1:1 in the central pixel of the radial data. This situation could be substantially improved by employing a quadrature design radiofrequency coil and reducing the diameter of that coil. Preliminary estimates of signal-to-noise ratios in NMR are notoriously difficult and probably only accurate to within a factor of two or three; nevertheless, the above estimates suggest that sufficient signal-to-noise ratios in the NMR signal could be obtained with a low-field (10 MHz, or 0.2 T) instrument for rapid rheometry based on the projection and DIAT techniques discussed above.

ACKNOWLEDGMENTS

The authors thank Dr. Herchel Smith for an endowment which provided the facilities; Dr. T. Adrian Carpenter and Messrs. Cliff Bunch and Simon Smith for technical assistance with the NMR spectrometer; Dr. Nicholas J. Herrod for providing data visualization software; and Dr. A. R. C. Gates and Mr. R. G. Wise for stimulating discussions.

REFERENCES

1. S. J. Gibbs, D. Xing, S. Ablett, I. D. Evans, W. J. Frith, D. E. Haycock, T. A. Carpenter, and L. D. Hall, *J. Rheol.* **38,** 1757 (1994).
2. K. R. Jeffrey, P. T. Callaghan, and Y. Xia, *Food Res. Int.* **27,** 199 (1994).
3. S. J. Gibbs, K. L. James, L. D. Hall, S. Ablett, W. J. Frith, and D. E. Haycock, *J. Rheol.* **40,** 425 (1996).
4. S. A. Altobelli, R. C. Givler, and E. Fukushima, *J. Rheol.* **35,** 721 (1991).
5. J. Ding, R. W. Lyczkowski, W. T. Sha, S. A. Altobelli, and E. Fukushima, *Powder Technol.* **77,** 301 (1993).

6. D. N. Guilfoyle, P. Mansfield, P., and K. J. Packer, *J. Magn. Reson.* **97,** 342 (1992).
7. B. J. Pangrle, E. G. Walsh, S. C. Moore, and D. DiBiaso, *Chem. Eng. Sci.* **47,** 517 (1992).
8. K. Y. Chung, G. Belfort, W. A. Edelstein, and X. Li, *J. Mebr. Sci.* **81,** 151 (1993).
9. M. Nakagawa, S. A. Altobelli, A. Caprihan, E. Fukushima, and E.-K. Jeong, *Exp. Fluids* **16,** 54 (1993).
10. S. J. Gibbs, T. A. Carpenter, and L. D. Hall, *J. Magn. Reson. A* **105,** 209 (1993).
11. K. Fukuda, A. Inouye, Y. Kawabe, and A. Hirai, *J. Phys. Soc. Jpn.* **54,** 4555 (1985).
12. R. L. Powell, J. E. Maneval, J. D. Seymour, K. L. McCarthy, and M. J. McCarthy, *J. Rheol.* **38,** 1465 (1994).
13. C. J. Rofe, R. K. Lambert, and P. T. Callaghan, *J. Rheol.* **38,** 875 (1994).
14. Y. Wang, E. D. von Meerwall, *J. Non-Cryst. Solids* **172–174,** 1047 (1994).
15. J. E. Maneval, K. L. McCarthy, M. J. McCarthy, and R. L. Powell, U.S. Patent 5,532,593 (1996).
16. D. A. Grabowski and C. Schmidt, *Macromolecules* **27,** 2632 (1994).
17. A. Caprihan and E. Fukushima, *Phys. Rep.* **198,** 195 (1990).
18. M. A. Smith, *Clin. Phys. Physiol. Meas.* **11,** 101 (1990).
19. P. T. Callaghan and Y. Xia, *J. Magn. Reson.* **91,** 326 (1991).
20. E. O. Stejskal, *J. Chem. Phys.* **43,** 3597 (1965).
21. Callaghan, P. T. ''Principles of Nuclear Magnetic Resonance Microscopy,'' Clarendon Press, Oxford, 1991.
22. D. Xing, S. J. Gibbs, J. A. Derbyshire, E. J. Fordham, T. A. Carpenter, and L. D. Hall, *J. Magn. Reson. B* **106,** 1 (1995).
23. D. H. Wu, A. Chen, and C. S. Johnson, *J. Magn. Reson. A* **115,** 123 (1995).
24. R. G. Wise, B. Newling, A. R. C. Gates, D. Xing, T. A. Carpenter, and L. D. Hall, *Magn. Reson. Imaging* **14,** 173 (1996).
25. P. D. Majors and A. Caprihan, *J. Magn. Reson.* **94,** 225 (1991).
26. D. I. Hoult, C. N. Chen, and V. J. Sank, *Magn. Reson. Med.* **3,** 730 (1986).